

# Subnano $\text{Al}_2\text{O}_3$ Coatings for Kinetics and Stability Optimization of $\text{LiNi}_{0.83}\text{Co}_{0.12}\text{Mn}_{0.05}\text{O}_2$ via $\text{O}_3$ -Based Atomic Layer Deposition

Jiawei Li, Jianhua Wu, Mingxuan Wang, Di Wen, Xiao Liu,\* Bin Shan, and Rong Chen\*



Cite This: ACS Appl. Mater. Interfaces 2025, 17, 3205–3213



Read Online

ACCESS |

Metrics & More

Article Recommendations

Supporting Information

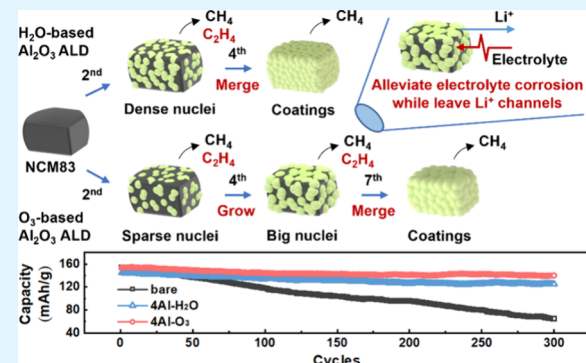
**ABSTRACT:** The Ni-rich  $\text{LiNi}_x\text{Co}_y\text{Mn}_{1-x-y}\text{O}_2$  cathode (NCM,  $x \geq 0.6$ ) suffers rapid capacity decay due to serious surface degradations from the corrosion of the electrolyte. The processes of the  $\text{H}_2\text{O}$ - and  $\text{O}_3$ -based  $\text{Al}_2\text{O}_3$  atomic layer deposition (ALD) on the single-crystal  $\text{LiNi}_{0.83}\text{Co}_{0.12}\text{Mn}_{0.05}\text{O}_2$  (NCM83) are investigated by *in situ* measurements to understand the mechanism of their different impacts on the electrochemical performance of NCM83.  $\text{C}_2\text{H}_4$  is found only produced during the trimethyl aluminum (TMA) chemisorption on NCM83 while not produced during TMA chemisorption on  $\text{LiOH}$  and  $\text{Li}_2\text{CO}_3$  impurities or deposited  $\text{Al}_2\text{O}_3$ . As an indicator, the disappearance of  $\text{C}_2\text{H}_4$  indicates that NCM83 is totally covered by four monolayers of  $\text{Al}_2\text{O}_3$  via the  $\text{H}_2\text{O}$ -based ALD while seven monolayers of  $\text{Al}_2\text{O}_3$  via the  $\text{O}_3$ -based ALD, which is owing to the  $\text{O}_3$ -based  $\text{Al}_2\text{O}_3$  ALD undergoing a longer growth period from the nuclei to continuous coatings on NCM83 due to a lower nucleation and growth rate. At the same monolayers of  $\text{Al}_2\text{O}_3$ , the  $\text{O}_3$ -based ALD-coated NCM83 cathode shows better rate and cycling performance than the  $\text{H}_2\text{O}$ -based ALD-coated NCM83 cathode, which is attributed to higher  $\text{Li}^+$  diffusivity of NCM83 due to the more pristine surface of NCM83 exposed for the  $\text{Li}^+$  transfer and fewer surface and crystal degradations of NCM83 due to more robust coatings. The  $\text{O}_3$ -based ALD-coated NCM83 cathode with four monolayers of  $\text{Al}_2\text{O}_3$  achieves the best balance of the rate and cycling performance, which almost retains the rate performance of the pristine NCM83 cathode and remarkably improves the cycling stability of pristine NCM83 cathodes from 42.1 to 91.2% after 300 cycles at 3.0–4.5 V and 1 C.

**KEYWORDS:** atomic layer deposition,  $\text{Al}_2\text{O}_3$  coatings, film growth, cathode materials, lithium-ion batteries

## 1. INTRODUCTION

Cycling stability remarkably influences the lifespan of lithium-ion batteries, which are extraordinarily significant and draw abundant concerns in academia and industry.<sup>1,2</sup> The irreversible reactions between the cathode and electrolyte induce decrements of active lithium and increments of interface resistance due to the depositions of byproducts on the surface of the cathode, consumptions of the electrolyte, transition metal ion dissolution, and surface phase transition of the cathodes, which are key factors for the capacity decay of the battery.<sup>3–7</sup> Coatings serve as barriers to avoid direct contact between the cathode and electrolyte, which have been proven to be able to improve the cycling stability of the cathode by alleviating surface side reactions.<sup>8–12</sup>

Atomic layer deposition (ALD), with the nature of self-limited surface reactions, is an ideal method for building uniform ultrathin coatings.<sup>8,13</sup> Numerous materials, such as  $\text{Al}_2\text{O}_3$ ,<sup>14–22</sup>  $\text{ZrO}_2$ ,<sup>23–25</sup>  $\text{TiO}_2$ ,<sup>26,27</sup>  $\text{B}_2\text{O}_3$ ,<sup>28</sup>  $\text{V}_2\text{O}_5$ ,<sup>29</sup>  $\text{LiAlF}_4$ ,<sup>30</sup>  $\text{LiAlO}_2$ ,<sup>31,32</sup> AlPON,<sup>33</sup> and TiPON,<sup>34</sup> had been coated on the cathodes via ALD, which improved the electrochemical stability of the cathodes.  $\text{Al}_2\text{O}_3$  was the most widely used material among them due to good electrochemical stability,



easy manufacture, and low price, which had been used to stabilize multiple cathodes, such as  $\text{LiCoO}_2$ ,<sup>14,15</sup>  $\text{LiNi}_x\text{Co}_y\text{Mn}_{1-x-y}\text{O}_2$ ,<sup>16,17</sup>  $\text{LiMn}_2\text{O}_4$ ,<sup>18</sup>  $\text{LiNi}_{0.5}\text{Mn}_{1.5}\text{O}_4$ ,<sup>19</sup>  $\text{LiFePO}_4$ ,<sup>20</sup> S,<sup>21</sup> Li- and Mn-rich cathodes,<sup>22</sup> etc. It was reported that only a few monolayers of  $\text{Al}_2\text{O}_3$  could effectively improve the cycling stability of the cathode.<sup>14,15</sup> As the thickness of  $\text{Al}_2\text{O}_3$  further increased, the cycling stability of the cathode only slightly increased, while the rate capability sharply decreased. To observe surface species variation during the  $\text{Al}_2\text{O}_3$  ALD process on the surface of  $\text{LiNi}_{1/3}\text{Co}_{1/3}\text{Mn}_{1/3}\text{O}_2$ , top surface characterization methods like low-energy ion scattering (LEIS) and time-of-flight secondary ion mass spectroscopy (ToF-SIMS) were used to characterize the content variation of the surface species, which indicated that  $\text{LiNi}_{1/3}\text{Co}_{1/3}\text{Mn}_{1/3}\text{O}_2$  was totally covered by about 10–15

Received: September 5, 2024

Revised: December 5, 2024

Accepted: December 23, 2024

Published: January 2, 2025



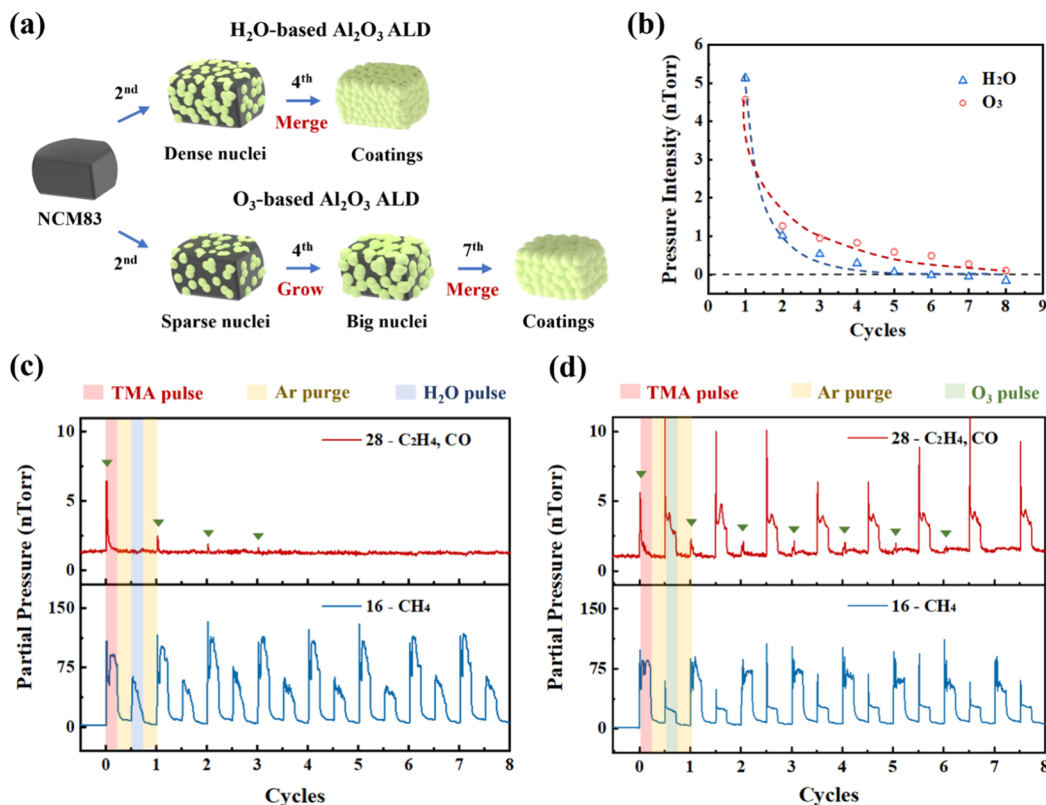


**Figure 1.** (a)  $\text{Al}_2\text{O}_3$  nucleation and growth process of the  $\text{H}_2\text{O}$ - and  $\text{O}_3$ -based  $\text{Al}_2\text{O}_3$  ALD on the NCM83 particles, (b) maximum pressure intensity of  $\text{C}_2\text{H}_6$  in each TMA pulse during the  $\text{H}_2\text{O}$ - and  $\text{O}_3$ -based  $\text{Al}_2\text{O}_3$  ALD on the NCM83 particles, and *in situ* QMS measurements of the (c)  $\text{H}_2\text{O}$ - and (d)  $\text{O}_3$ -based  $\text{Al}_2\text{O}_3$  ALD on the NCM83 particles.

monolayers of  $\text{Al}_2\text{O}_3$ .<sup>35</sup> Another method with atomic-sampling depth for the detection of surface species variation was proposed by measuring the special byproducts during the  $\text{Al}_2\text{O}_3$  ALD process via the mass spectrometer.  $\text{C}_2\text{H}_6$  was reported to be only produced during trimethyl aluminum (TMA) chemisorption on the surface of  $\text{LiMn}_2\text{O}_4$  while not produced during TMA chemisorption on deposited  $\text{Al}_2\text{O}_3$ , which could serve as an indicator for the exposed surface of pristine  $\text{LiMn}_2\text{O}_4$ .<sup>36</sup> The production of  $\text{C}_2\text{H}_6$  gradually declined as  $\text{Al}_2\text{O}_3$  ALD cycles increased, which indicated that the surface of  $\text{LiMn}_2\text{O}_4$  was gradually covered by  $\text{Al}_2\text{O}_3$ . Besides, TMA was reported to reduce the surface  $\text{Mn}^{4+}$  into  $\text{Mn}^{3+}$  of  $\text{LiMn}_2\text{O}_4$  during the  $\text{Al}_2\text{O}_3$  ALD process. TMA was also reported to reduce the surface transition metal ions of  $\text{LiCoO}_2$ ,  $\text{LiNi}_{0.5}\text{Co}_{0.2}\text{Mn}_{0.3}\text{O}_2$ ,  $\text{LiNi}_{0.8}\text{Co}_{0.1}\text{Mn}_{0.1}\text{O}_2$ ,  $\text{LiNiO}_2$ , and  $0.35\text{Li}_2\text{MnO}_3\cdot0.65\text{LiNi}_{0.35}\text{Mn}_{0.45}\text{Co}_{0.2}\text{O}_2$  during the  $\text{Al}_2\text{O}_3$  ALD process.<sup>37,38</sup> However, no special byproducts were reported to be detected during the  $\text{Al}_2\text{O}_3$  ALD on these cathode materials. As the  $\text{Al}_2\text{O}_3$  film growth dramatically influenced the electrochemical performance of the cathode materials, the  $\text{Al}_2\text{O}_3$  film growth mode of different ALD processes deserved to be investigated.  $\text{O}_3$  was another available co-reactant used in the  $\text{Al}_2\text{O}_3$  ALD process, which exhibited different reaction mechanisms with TMA compared to  $\text{H}_2\text{O}$ . Besides, it gave less impurities to deposited  $\text{Al}_2\text{O}_3$ .<sup>39–43</sup> To the best of our knowledge,  $\text{O}_3$  had not been reported to be used in  $\text{Al}_2\text{O}_3$  ALD for coating cathode materials. Hence, it is worth investigating the  $\text{Al}_2\text{O}_3$  film growth of the  $\text{O}_3$ -based ALD on cathode materials and its impact on the electrochemical performance of the cathode materials.

Herein, we investigate the  $\text{H}_2\text{O}$ - and  $\text{O}_3$ -based  $\text{Al}_2\text{O}_3$  ALD processes on NCM83 and their impact on the electrochemical performance of the NCM83 cathode. *In situ* quadrupole mass spectrometry (QMS) is used to monitor the byproducts of the  $\text{Al}_2\text{O}_3$  ALD on NCM83. An *in situ* quartz crystal microbalance (QCM) is used to measure the mass variation of  $\text{Al}_2\text{O}_3$  growth on NCM83. Surface characterizations are performed to detect variation of the surface species after the  $\text{Al}_2\text{O}_3$  ALD process. The electrochemical tests are performed to evaluate the performance of the ALD  $\text{Al}_2\text{O}_3$ -coated NCM83 cathode. The NCM83 cathodes obtained from the cycled coin cells are characterized to compare and analyze their degradations.

## 2. EXPERIMENTAL SECTION

**2.1. Material Preparation.** NCM83 was synthesized by calcining the mixture of the  $\text{LiOH}\cdot\text{H}_2\text{O}$  and  $\text{Ni}_{0.83}\text{Co}_{0.12}\text{Mn}_{0.05}(\text{OH})_2$  particles with a molar ratio of 1.04:1 at a temperature of 500 °C for 5 h initially and then at a temperature of 850 °C for 12 h.

$\text{Al}_2\text{O}_3$  coating was prepared directly on NCM83 particles using a homemade fluidized-bed ALD reactor.  $\text{Al}_2\text{O}_3$  was deposited at 120 °C using TMA (Aimou Yuan, Nanjing, China) and  $\text{H}_2\text{O}$  or  $\text{O}_3$  as precursors. In a typical  $\text{Al}_2\text{O}_3$  ALD cycle, a 90 s TMA pulse, 120 s Ar purge, 90 s  $\text{H}_2\text{O}$  or  $\text{O}_3$  pulse, and 120 s Ar purge were alternately operated.  $\text{O}_3$  was prepared with high-purity oxygen through an  $\text{O}_3$  generator. The NCM83 particles coated with  $\text{Al}_2\text{O}_3$  in 0, 2, 4, and 8 ALD cycles were named as bare, 2Al– $\text{H}_2\text{O}$ , 2Al– $\text{O}_3$ , 4Al– $\text{H}_2\text{O}$ , 4Al– $\text{O}_3$ , 8Al– $\text{H}_2\text{O}$ , and 8Al– $\text{O}_3$  NCM83 particles.

**2.2. Material Characterizations.** The concentration of Al in NCM83 particles was measured via inductively coupled plasma optical emission spectroscopy (ICP–OES) with an Avio 220 Max instrument from PerkinElmer. The mass uptake during the  $\text{Al}_2\text{O}_3$  ALD process was measured using a QCM with a SQM-160 instrument from Inficon. For QCM preparation, NCM83 particles

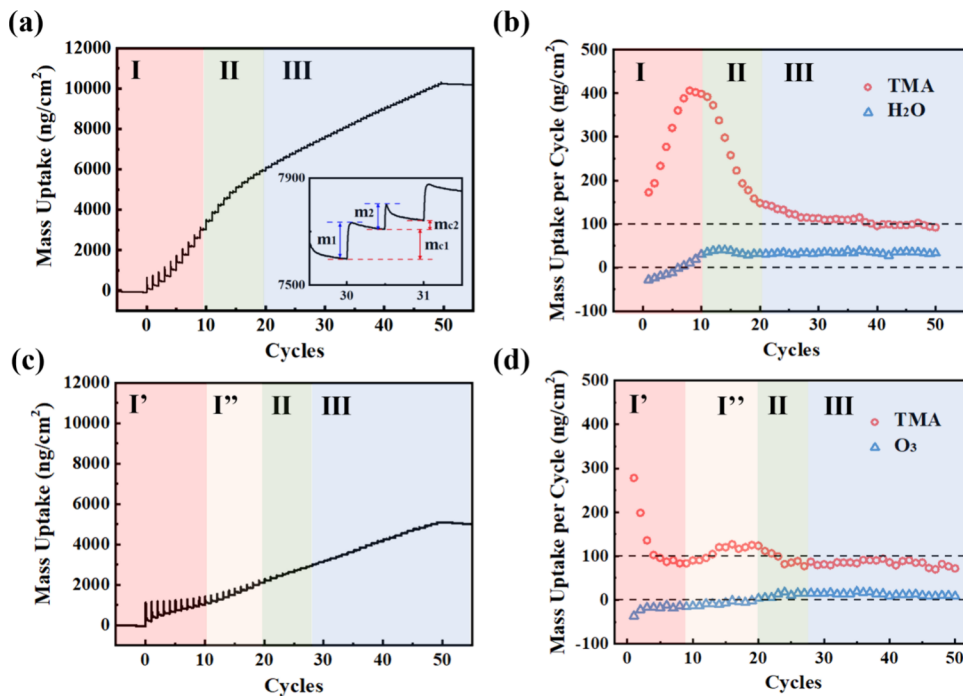


**Figure 2.** *In situ* QCM measurements of the  $\text{Al}_2\text{O}_3$  ALD process on the QCM sensor loaded with NCM83 particles: (a) mass uptake and (b) mass uptake of chemisorbed TMA and  $\text{H}_2\text{O}$  per cycle during the  $\text{H}_2\text{O}$ -based  $\text{Al}_2\text{O}_3$  ALD process on the NCM83 particle bed, with the inset being an enlarged view of QCM measurements of the  $\text{H}_2\text{O}$ -based  $\text{Al}_2\text{O}_3$  ALD process on the NCM83 particle bed, (c) mass uptake and (d) mass uptake of chemisorbed TMA and  $\text{O}_3$  per cycle during the  $\text{O}_3$ -based  $\text{Al}_2\text{O}_3$  ALD on the NCM83 particle bed.

were loaded on the QCM sensor as a particle bed. NCM83 particles were dispersed in ethanol to make the suspension first, and then the suspension was sprayed on the QCM sensor. Finally, a drying procedure was performed to obtain the QCM sensor loaded with NCM83 particles. For QCM measurement, a 1 s TMA pulse, 30 s Ar purge, 1 s  $\text{H}_2\text{O}$  or  $\text{O}_3$  pulse, and 30 s Ar purge were alternately operated. The byproducts during the  $\text{Al}_2\text{O}_3$  ALD process were measured by a quadrupole mass spectrometer (QMS) with a Dycor LC-D200 instrument from AMETEK. The crystal structures of the NCM83 particles and cathodes were characterized using an Empyrean (PANalytical B.V.) X-ray diffractometer (XRD) with a Cu  $\text{K}\alpha$  radiation source. The morphologies of the NCM83 particles and cathodes were observed by scanning electron microscopy (SEM) with a Quanta650 FEG instrument from FEI. The surface compositions of the NCM83 particles and cathodes were detected by time-of-flight secondary ion mass spectrometry (ToF-SIMS) with a Helios 5 instrument and X-ray photoelectron spectroscopy (XPS) with a K-Alpha instrument from Thermo Scientific Co. All XPS spectra were calibrated by aligning the C 1s peak to 285 eV. For electronic conductivity measurements, NCM83 particles were compressed in a mold at a pressure of 20 MPa and subsequently measured by a multimeter.

**2.3. Electrochemical Measurements.** The NCM83 cathode slurry was formulated with NCM83, carbon black, and poly(vinylidene fluoride) (PVDF) in a weight ratio of 8:1:1, using a *N*-methyl pyrrolidone (NMP)-based solution. The NCM83 cathode slurry was coated on aluminum foil and then dried at 120 °C. The NCM83 loading was around 3 mg/cm<sup>2</sup>. The electrolyte consisted of 1 M LiPF<sub>6</sub> dissolved in a solvent mixture of ethyl methyl carbonate, ethylene carbonate, and dimethyl carbonate in a ratio of 1:1:1 by volume. The coin cell was assembled in a glovebox filled with argon using a porous polypropylene separator, a lithium anode, and a NCM83 cathode. Charge-discharge tests were performed using a battery tester (Land CT3002A), operating within a voltage range of 3.0–4.5 V. The tests were conducted at a current density, where 1 C corresponds to 200 mA/g, and at a temperature of 19 °C. Storage tests were carried out at 19 °C for 230 h after the coin cells were charged to 4.05 V at a current density of 0.1 C using the Land

CT3002A tester. The galvanostatic intermittent titration technique (GITT) was also performed using a battery tester (Land CT3002A), where the coin cells were subjected to a 0.1 C current for 20 min and then rested for 60 min. Electrochemical impedance spectroscopy (EIS) was measured with an electrochemical workstation with an Autolab PGSTAT302N instrument from Metrohm. The frequency range was set from 100 kHz to 0.01 Hz, and the perturbation amplitude was set to ±5 mV.

### 3. RESULTS AND DISCUSSION

Figure 1a illustrates the  $\text{Al}_2\text{O}_3$  nucleation and growth process of the  $\text{H}_2\text{O}$ - and  $\text{O}_3$ -based  $\text{Al}_2\text{O}_3$  ALD on the NCM83 particles (Ni, Co, and Mn contents of NCM83 shown in Table S1 of the Supporting Information). As shown in Figure 1b, the maximum pressure intensity of  $\text{C}_2\text{H}_4$  gradually decreases as the number of  $\text{Al}_2\text{O}_3$  ALD cycles increases. The maximum pressure intensity of  $\text{C}_2\text{H}_4$  reaches zero after 4  $\text{H}_2\text{O}$ -based  $\text{Al}_2\text{O}_3$  ALD cycles, while the maximum pressure intensity of  $\text{C}_2\text{H}_4$  reaches zero after 7  $\text{O}_3$ -based  $\text{Al}_2\text{O}_3$  ALD cycles, which indicates that the surface of NCM83 particles is totally covered by  $\text{Al}_2\text{O}_3$  after 4  $\text{H}_2\text{O}$ -based  $\text{Al}_2\text{O}_3$  ALD cycles while totally covered by  $\text{Al}_2\text{O}_3$  after 7  $\text{O}_3$ -based  $\text{Al}_2\text{O}_3$  ALD cycles. Figure 1c shows the *in situ* QMS measurements of the  $\text{H}_2\text{O}$ -based  $\text{Al}_2\text{O}_3$  ALD process on NCM83 particles. In the first TMA pulse,  $\text{C}_2\text{H}_4$  with a molecular mass of 28 and  $\text{CH}_4$  with a molecular mass of 16 occur, which are attributed to the byproducts of the TMA chemisorption on the NCM83 particles.  $\text{C}_2\text{H}_4$  may be the byproduct of the TMA chemisorption on surface  $-\text{O}$  of NCM83, while  $\text{CH}_4$  is the byproduct of the TMA chemisorption on surface  $-\text{OH}$  of NCM83. In the second TMA pulse, the partial pressure of  $\text{C}_2\text{H}_4$  sharply decreases, which is attributed to the fact that most of the surface of the NCM83 particles is covered by  $\text{Al}_2\text{O}_3$  during the first  $\text{Al}_2\text{O}_3$  ALD cycles. Different from  $\text{C}_2\text{H}_4$ ,

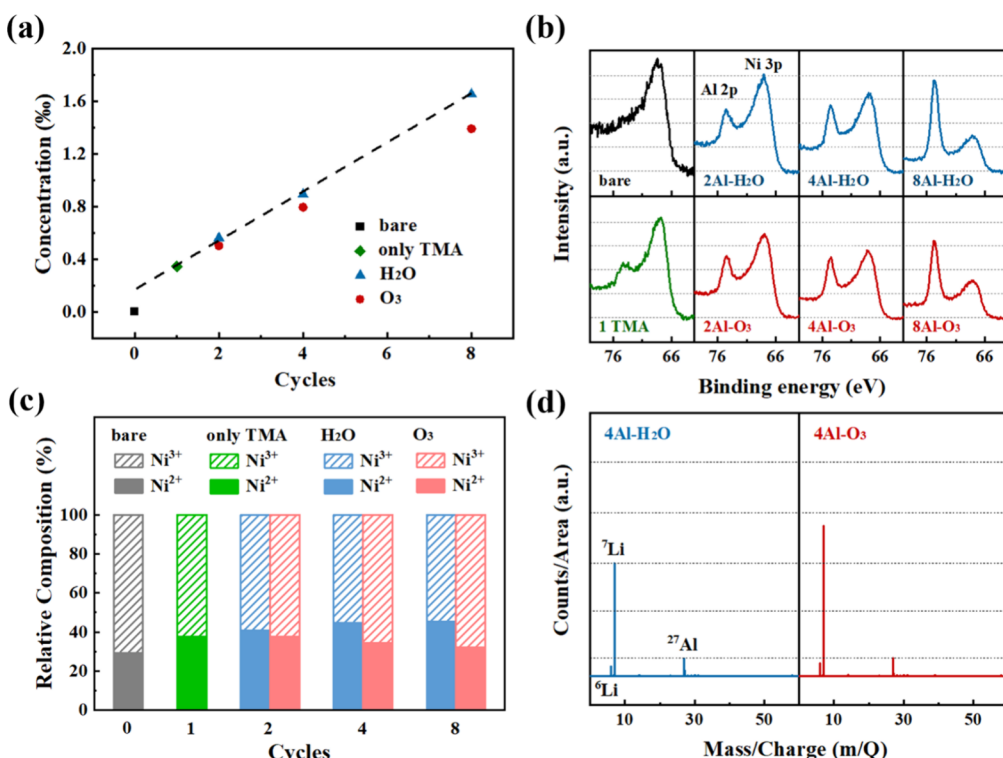


**Figure 3.** (a) ICP results, (b) Al 2p and Ni 3p XPS spectra, and (c) Al/Ni relative composition of the bare, single TMA pulse-treated, H<sub>2</sub>O- and O<sub>3</sub>-based Al<sub>2</sub>O<sub>3</sub>-coated NCM83 particles and (d) TOF-SIMS spectra of the 4Al-H<sub>2</sub>O and 4Al-O<sub>3</sub> NCM83 particles.

the partial pressure of  $\text{CH}_4$  is kept, which is attributed to  $\text{CH}_4$  also being produced during the TMA chemisorption on deposited  $\text{Al}_2\text{O}_3$ . After 4  $\text{Al}_2\text{O}_3$  ALD cycles,  $\text{C}_2\text{H}_4$  disappears, which indicates that the surface of the NCM83 particles is totally covered by  $\text{Al}_2\text{O}_3$ . The disappearance of  $\text{C}_2\text{H}_4$  may be attributed to the fact that  $\text{C}_2\text{H}_4$  cannot chemisorb on surface  $-\text{O}$  of  $\text{Al}_2\text{O}_3$  due to Al not possessing variable valence like transition metals. Figure 1d shows the *in situ* QMS measurements of the  $\text{O}_3$ -based  $\text{Al}_2\text{O}_3$  ALD process on the NCM83 particles. Similar phenomena are observed in the first and second TMA pulses. While different phenomena occur in the subsequent TMA pulses, the decline rate of  $\text{C}_2\text{H}_4$  is slow, which indicates that the residual exposed surface of NCM83 is gradually being covered at a lower rate. Figure S1 of the Supporting Information shows almost the same phenomena when the  $\text{Al}_2\text{O}_3$  ALD process is performed at 180 °C. Figure S2 of the Supporting Information shows that TMA occurs at the later stage of each TMA pulse, indicating saturation chemisorption of TMA on the NCM83 particles in each TMA pulse, to exclude the possibility that  $\text{C}_2\text{H}_4$  is produced by TMA reacting with lithium impurities ( $\text{LiOH}$  and  $\text{Li}_2\text{CO}_3$ ) on the surface of NCM83. *In situ* QMS measurements of  $\text{Al}_2\text{O}_3$  ALD on the  $\text{LiOH}$  and  $\text{Li}_2\text{CO}_3$  particles using  $\text{H}_2\text{O}$  or  $\text{O}_3$  as the co-reactant are shown in Figure S3 of the Supporting Information, which exhibits that no  $\text{C}_2\text{H}_4$  occurs during the TMA pulse. Besides, although the molecular mass of CO is the same as  $\text{C}_2\text{H}_4$ , CO should not be produced during the TMA pulse due to the lack of oxygen. CO is produced during the pulsed  $\text{O}_3$  pulse.

*In situ* QCM measurements are performed to probe the growth of ALD Al<sub>2</sub>O<sub>3</sub> on the NCM83 particle bed. The schematic illustration of the H<sub>2</sub>O- and O<sub>3</sub>-based Al<sub>2</sub>O<sub>3</sub> ALD process on the NCM83 particle bed is shown in Figure S4 of

the Supporting Information. Figure 2a shows that the mass uptake rate of  $\text{Al}_2\text{O}_3$  is fast initially, then decreases, and finally remains steady at a low value during the  $\text{H}_2\text{O}$ -based  $\text{Al}_2\text{O}_3$  ALD process on the NCM83 particle bed. The inset shows the detailed mass uptake during an ALD cycle, where  $m_1$  and  $m_2$  are the mass uptakes from the physisorption and chemisorption of TMA and  $\text{H}_2\text{O}$ . As physisorbed TMA and  $\text{H}_2\text{O}$  gradually desorb, the final mass uptake of  $m_{c1}$  and  $m_{c2}$  is from chemisorbed TMA and  $\text{H}_2\text{O}$ . The reduction of the  $\text{Al}_2\text{O}_3$  mass uptake rate is attributed to the decreased surface area evidenced by decreased physisorption of TMA (shown in Figure S5a of the Supporting Information), which is attributed to the voids in the NCM83 particle bed being gradually filled by  $\text{Al}_2\text{O}_3$ . Figure 2b shows the mass uptake of chemisorbed TMA and  $\text{H}_2\text{O}$  from each  $\text{Al}_2\text{O}_3$  ALD cycle. The process can be divided into three stages. In the first stage, the mass uptake of chemisorbed TMA increases, which is attributed to  $\text{Al}_2\text{O}_3$  undergoing a process from the nuclei to continuous coatings. Besides, the mass uptake of chemisorbed  $\text{H}_2\text{O}$  changes from negative to positive, which indicates that the surface reaction mechanism changes due to surface substances transforming from NCM83 into  $\text{Al}_2\text{O}_3$ . More ALD cycles were observed for the  $\text{Al}_2\text{O}_3$  nucleation on NCM83 from the QCM results than from the QMS results, attributed to the unsaturated chemisorption of TMA and  $\text{H}_2\text{O}$  on the subsurface NCM83 particle bed in the QCM measurements. In the second and third stages, the mass uptake of TMA gradually decreases and is finally steady at a low value, as explained above. Figure 2c shows the mass uptake rate of  $\text{Al}_2\text{O}_3$  during the  $\text{O}_3$ -based  $\text{Al}_2\text{O}_3$  ALD process on the NCM83 particle bed, which is lower compared to that during the  $\text{H}_2\text{O}$ -based  $\text{Al}_2\text{O}_3$  ALD process. Figure 2d shows the mass uptake of chemisorbed TMA and  $\text{O}_3$  from each  $\text{Al}_2\text{O}_3$  ALD cycle. The process can

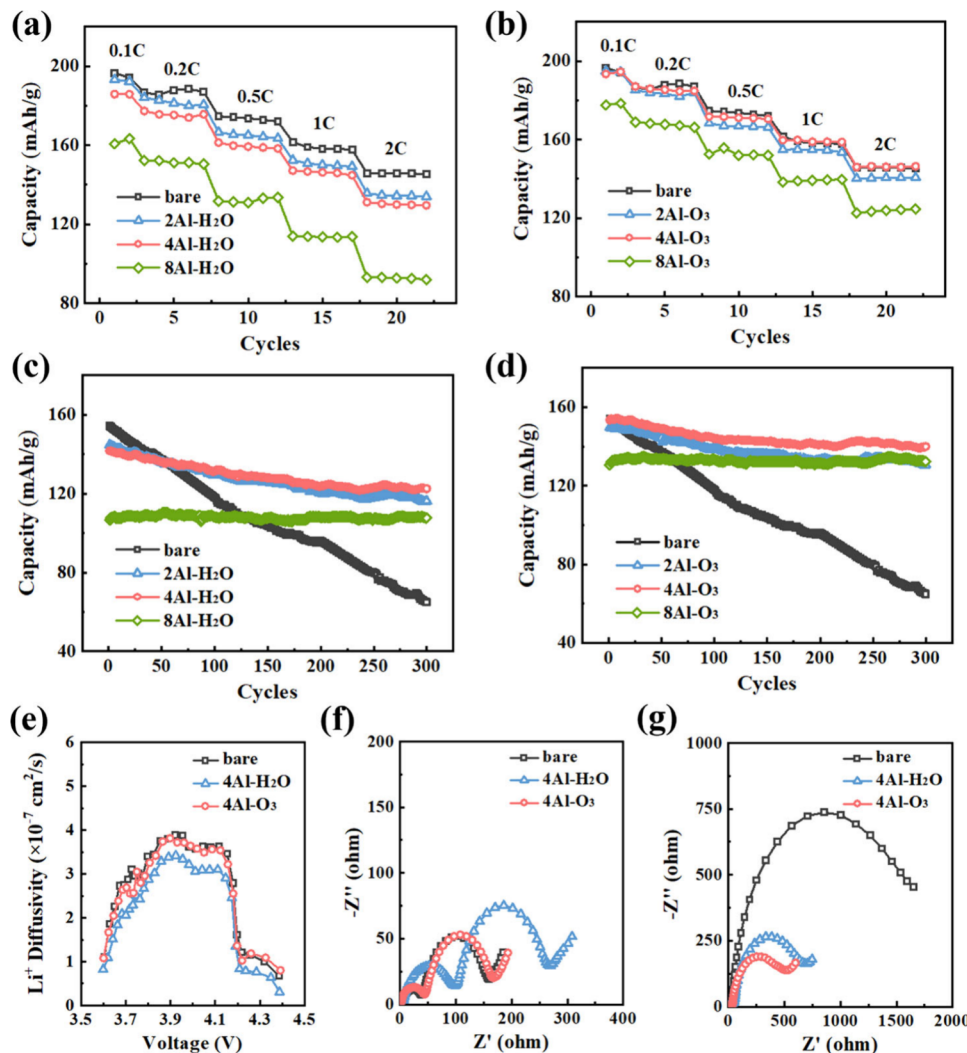


**Figure 4.** Rate capability of the (a)  $\text{H}_2\text{O}$ -based ALD  $\text{Al}_2\text{O}_3$ -coated NCM83 cathodes and (b)  $\text{O}_3$ -based ALD  $\text{Al}_2\text{O}_3$ -coated NCM83 cathodes, cycling stabilities of the (c)  $\text{H}_2\text{O}$ -based ALD  $\text{Al}_2\text{O}_3$ -coated NCM83 cathodes and (d)  $\text{O}_3$ -based ALD  $\text{Al}_2\text{O}_3$ -coated NCM83 cathodes, (e)  $\text{Li}^+$  diffusivity of the bare, 4Al- $\text{H}_2\text{O}$ , and 4Al- $\text{O}_3$  NCM83 cathodes, and EIS of the bare, 4Al- $\text{H}_2\text{O}$ , and 4Al- $\text{O}_3$  NCM83 cathodes after the (f) 2nd and (g) 300th cycles at the charged state.

also be divided into three stages, and the first stage can be divided into two substages. In the first substage, the mass uptake of TMA gradually decreases, which indicates that the surface-available TMA chemisorbed sites of NCM83 decrease. It may be attributed to  $\text{O}_3$  lacking the ability to create hydroxyl sites on pristine NCM83 for TMA chemisorption compared to  $\text{H}_2\text{O}$ . As  $\text{Al}_2\text{O}_3$  nucleates and grows, the  $\text{Al}_2\text{O}_3$  nuclei can serve as the substrate for TMA chemisorption. Hence, the mass uptake of chemisorbed TMA increases until continuous  $\text{Al}_2\text{O}_3$  coatings form in the second substage. The higher mass uptake of chemisorbed TMA in the first TMA pulse shown in Figure 2d than in Figure 2b is attributed to the higher surface area of the loaded NCM83 particle bed evidenced by higher physisorption (shown in Figure S5b of the Supporting Information). In the second and third stages, the mass uptake of TMA gradually decreases and finally steadies at a low value, which is similar to the trend during the  $\text{H}_2\text{O}$ -based  $\text{Al}_2\text{O}_3$  ALD process on the NCM83 particle bed. The difference is that the steady mass uptake from chemisorbed TMA during the  $\text{O}_3$ -based  $\text{Al}_2\text{O}_3$  ALD process is lower than that from chemisorbed TMA during the  $\text{H}_2\text{O}$ -based  $\text{Al}_2\text{O}_3$  ALD process in the final

stage, which is attributed to fewer surface-available sites for TMA chemisorption. Besides, the mass uptake of  $\text{Al}_2\text{O}_3$  during the  $\text{H}_2\text{O}$ - or  $\text{O}_3$ -based  $\text{Al}_2\text{O}_3$  ALD process on the NCM83 particle bed is similar to the mass uptake of that on the bare QCM sensor (shown in Figure S6 of the Supporting Information), which further validates  $\text{Al}_2\text{O}_3$  having totally covered the surface of NCM83 particles and filled voids in the NCM83 particle bed in the third stage.

To briefly evaluate the  $\text{Al}_2\text{O}_3$  ALD growth rate on the NCM83 particles, ICP-OES is used to measure the content of Al in the NCM83 particles (shown in Figure 3a). As the number of  $\text{Al}_2\text{O}_3$  ALD cycles increases, the Al concentration gradually increases. The growth curve of the  $\text{H}_2\text{O}$ -based  $\text{Al}_2\text{O}_3$  ALD shows good linearity while not passing through the origin, which is attributed to excess  $\text{Al}_2\text{O}_3$  being attached to the NCM83 particles due to the bulk reactions between TMA and surface  $\text{LiOH}$  of the NCM83 particles (Figure S7 and Table S2 of the Supporting Information). No excess mass uptake is observed in the QCM results during the first TMA pulse, which is attributed to surface  $\text{LiOH}$  of the NCM83

particles being dissolved into ethanol during the preparation process of loading NCM83 particles on the QCM. Besides, no nucleation stage is observed in the ICP results, which is attributed to sufficient hydroxylation for NCM83 during the H<sub>2</sub>O pulse, which is owing to the good gas–solid contact in the fluidization particle bed compared to the static particle bed loaded on the QCM sensor. The growth rate of Al<sub>2</sub>O<sub>3</sub> on the NCM83 particles from the O<sub>3</sub>-based Al<sub>2</sub>O<sub>3</sub> ALD is lower than that from the H<sub>2</sub>O-based Al<sub>2</sub>O<sub>3</sub> ALD. Figure S8 of the Supporting Information shows that a higher temperature of 180 °C does not change the growth rate of Al<sub>2</sub>O<sub>3</sub> on the NCM83 particles. XPS characterizations are performed to measure the relative composition of Al and Ni on the surface of the NCM83 particles. No Al 2p peak is observed on the bare NCM83 particles (shown in Figure 3b). After a single TMA pulse, the Al 2p peak occurs. As Al<sub>2</sub>O<sub>3</sub> ALD cycles increase, the intensity of the Al 2p peak for both O<sub>3</sub>- and H<sub>2</sub>O-based Al<sub>2</sub>O<sub>3</sub>-coated NCM83 gradually increases and the intensity of the Ni 3p peak for both O<sub>3</sub>- and H<sub>2</sub>O-based Al<sub>2</sub>O<sub>3</sub>-coated NCM83 gradually decreases. Figure 3c shows the relative compositions of Ni<sup>3+</sup> and Ni<sup>2+</sup> derived from the Ni 2p XPS spectra (Figure S9 of the Supporting Information). It shows that the content of Ni<sup>3+</sup> decreases while the content of Ni<sup>2+</sup> increases after a single TMA pulse, which indicates that TMA reduces surface Ni<sup>3+</sup> into Ni<sup>2+</sup>. Using H<sub>2</sub>O as the co-reactant, as the ALD cycles change from 2 to 4, surface Ni<sup>3+</sup> is further reduced to Ni<sup>2+</sup>. As the ALD cycles change from 4 to 8, the content of surface Ni<sup>3+</sup> barely changes, which is attributed to the surface of NCM83 being totally covered by Al<sub>2</sub>O<sub>3</sub>. Using O<sub>3</sub> as the co-reactant, the content of surface Ni<sup>2+</sup> of NCM83 is lower compared to using H<sub>2</sub>O as the co-reactant at the same Al<sub>2</sub>O<sub>3</sub> ALD cycles, which is attributed to O<sub>3</sub> oxidizing Ni<sup>2+</sup> into Ni<sup>3+</sup>. As the ALD cycles increase from 2 to 8, surface Ni<sup>2+</sup> is further oxidized into Ni<sup>3+</sup>, which is attributed to the surface of NCM83 not being totally covered by Al<sub>2</sub>O<sub>3</sub>. To observe the top surface species of NCM83, TOF-SIMS is performed on the marked regions (Figure S10 of the Supporting Information). As shown in Figure 3d, the <sup>6</sup>Li, <sup>7</sup>Li, and <sup>27</sup>Al peaks are observed on both the 4Al–H<sub>2</sub>O and 4Al–O<sub>3</sub> NCM83 particles. The spectra of the 4Al–O<sub>3</sub> NCM83 particles show almost the same <sup>27</sup>Al peak intensity and a higher <sup>7</sup>Li peak intensity compared to the spectra of the 4Al–H<sub>2</sub>O NCM83 particles, which indicates that more surface Li ions are exposed for the 4Al–O<sub>3</sub> NCM83 particles. No <sup>58</sup>Ni is observed in any of the TOF-SIMS spectra, which is attributed to the low production rate of the Ni secondary ions.

To evaluate the effect of H<sub>2</sub>O- and O<sub>3</sub>-based Al<sub>2</sub>O<sub>3</sub> on the electrochemical performance of the NCM83 cathodes, electrochemical tests are performed to probe it. As shown in Figure 4a, the Al<sub>2</sub>O<sub>3</sub>-coated NCM83 cathodes show inferior initial capacity and rate capability compared to bare NCM83 cathodes. Moreover, as the ALD cycles increase, the capacity further decreases. The capacity reduction is slight when the ALD cycles increase from 0 to 4 while serious when the ALD cycles increase from 4 to 8, which is due to the polarization slightly increasing from 0 to 4 while rapidly increasing from 4 to 8 (Figure S11a of the Supporting Information). It is attributed to the continuous Al<sub>2</sub>O<sub>3</sub> coatings forming after 4 H<sub>2</sub>O-based Al<sub>2</sub>O<sub>3</sub> ALD cycles, which leaves no exposed NCM83 surface for Li ion transfer. Hence, it apparently increases the transfer resistance of the Li ions. As shown in Figure 4b, the O<sub>3</sub>-based Al<sub>2</sub>O<sub>3</sub>-coated NCM83 cathodes show better rate capability compared to the H<sub>2</sub>O-based Al<sub>2</sub>O<sub>3</sub>-

coated NCM83 cathodes at the same ALD cycles due to less polarization (Figure S11b of the Supporting Information). It is attributed to the fact that O<sub>3</sub>-based Al<sub>2</sub>O<sub>3</sub> gives lower coverage on the surface of the NCM83 cathodes compared to H<sub>2</sub>O-based Al<sub>2</sub>O<sub>3</sub> at the same ALD cycles, which alleviates the resistance to the transfer of the Li ions. Besides, the 4Al–O<sub>3</sub> NCM83 cathode shows better rate capability than the 2Al–O<sub>3</sub> NCM83 cathode, which may be attributed to the further oxidation for the surface Ni ions of NCM83 being advantageous to the rate capability of the NCM83 cathode.<sup>44</sup> Figure 4c shows the cycling stability of the bare and Al<sub>2</sub>O<sub>3</sub>-coated NCM83 cathodes. It shows that the cycling stability of the NCM83 cathodes increases as the ALD cycles increase. Although with inferior initial capacity compared to the bare NCM83 cathode, the 4Al–H<sub>2</sub>O NCM83 cathode shows the highest capacity after cycling. The capacity retention of the 4Al–H<sub>2</sub>O NCM83 cathode is 86.5%, which is much higher than the capacity retention of the bare NCM83 cathode (42.1%). In comparison to H<sub>2</sub>O-based ALD Al<sub>2</sub>O<sub>3</sub>-coated NCM83 cathodes, the O<sub>3</sub>-based ALD Al<sub>2</sub>O<sub>3</sub>-coated NCM83 cathodes show a similar cycling performance variation, while both the initial and final capacities of the NCM83 cathodes are higher (Figure 4d). The 4Al–O<sub>3</sub> NCM83 cathode shows almost the same initial capacity as the bare NCM83 cathode and the highest capacity after cycling. The 4Al–O<sub>3</sub> NCM83 cathode shows a capacity retention of 91.2%, which is not only higher than that of the 4Al–H<sub>2</sub>O NCM83 cathode but also excellent compared to other modified Ni-rich cathodes reported in the literature (Figure S12 and Table S3 of the Supporting Information). The 4Al–O<sub>3</sub> NCM83 cathode also shows better voltage stabilization during cycling (panels c and d of Figure S11 of the Supporting Information) and still shows a clear plateau after cycling (Figure S13 of the Supporting Information). Besides, the storage stability of the 4Al–O<sub>3</sub> NCM83 cathode is the best (Figure S14 of the Supporting Information). Moreover, a higher Al<sub>2</sub>O<sub>3</sub> ALD temperature at 180 °C gives no obvious impact on the rate capability and cycling stability of 4Al–H<sub>2</sub>O and 4Al–O<sub>3</sub> NCM83 cathodes compared to the Al<sub>2</sub>O<sub>3</sub> ALD temperature at 120 °C (Figure S15 of the Supporting Information). To further investigate the effect of the ALD Al<sub>2</sub>O<sub>3</sub> coatings on the rate capability of the NCM83 cathode, the GITT measurements are performed to probe the Li<sup>+</sup> diffusivity of the NCM83 cathode (Figure S16 of the Supporting Information). The Li<sup>+</sup> diffusivities of bare, 4Al–H<sub>2</sub>O, and 4Al–O<sub>3</sub> NCM83 cathodes are calculated from the GITT measurements, as shown in Figure 4e. The results show that the Li<sup>+</sup> diffusivity of the 4Al–H<sub>2</sub>O NCM83 cathode is lower than that of the bare NCM83 cathode, while the Li<sup>+</sup> diffusivity of the 4Al–O<sub>3</sub> NCM83 cathode is higher than that of the 4Al–H<sub>2</sub>O NCM83 cathode and almost the same as that of the bare NCM83 cathode. Besides, the 4Al–O<sub>3</sub> NCM83 particles show a slightly lower electronic conductivity than the 4Al–H<sub>2</sub>O NCM83 particles (Figure S17 of the Supporting Information). Hence, it could be concluded that a higher Li<sup>+</sup> diffusivity for the 4Al–O<sub>3</sub> NCM83 cathode is attributed to a lower barrier to the Li<sup>+</sup> transfer, which accounts for the better rate capability of the 4Al–O<sub>3</sub> NCM83 cathode. Panels f and g of Figure 4 show the EIS of bare, 4Al–H<sub>2</sub>O, and 4Al–O<sub>3</sub> NCM83 cathodes before and after cycling. The surface film impedance ( $R_f$ ) and charge transfer resistance ( $R_{ct}$ ) of the 4Al–H<sub>2</sub>O NCM83 cathode are higher than those of the bare cathode, while  $R_f$  and  $R_{ct}$  of the 4Al–O<sub>3</sub> NCM83 cathode are close to those of the bare NCM83 cathode before cycling.

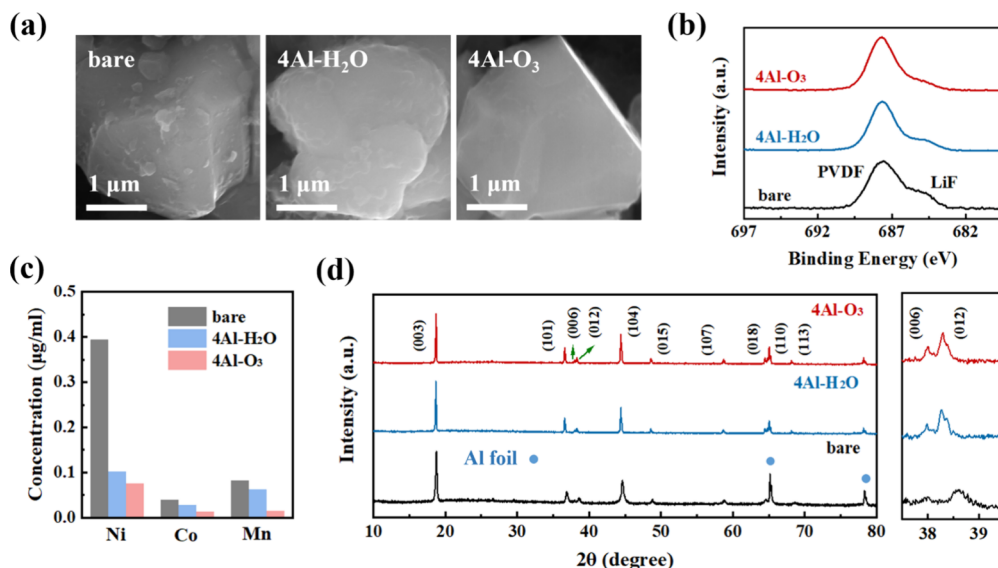


**Figure 5.** (a) SEM images of the cycled bare, 4Al–H<sub>2</sub>O, and 4Al–O<sub>3</sub> NCM83 cathodes, (b) F 1s XPS spectra of the cycled bare, 4Al–H<sub>2</sub>O, and 4Al–O<sub>3</sub> NCM83 cathodes, (c) ICP results from the anodes corresponding to the cycled bare, 4Al–H<sub>2</sub>O, and 4Al–O<sub>3</sub> NCM83 cathodes, and (d) XRD patterns of the cycled bare, 4Al–H<sub>2</sub>O, and 4Al–O<sub>3</sub> NCM83 cathodes.

(panels a and b of Figure S18 of the Supporting Information). The distribution of relaxation time (DRT) analysis further reveals that increased  $R_f$  and  $R_{ct}$  of the 4Al–H<sub>2</sub>O NCM83 cathode come from the extra electrochemical process due to the complete Al<sub>2</sub>O<sub>3</sub> coating (Figure S19 of the Supporting Information). After cycling,  $R_f$  of all of the NCM83 cathodes slightly decreases, while  $R_{ct}$  of all of the NCM83 cathodes remarkably increases (Figure S18c of the Supporting Information).  $R_{ct}$  of the bare NCM83 cathode is much higher than  $R_{ct}$  of the 4Al–H<sub>2</sub>O and 4Al–O<sub>3</sub> NCM83 cathodes, and  $R_{ct}$  of the 4Al–O<sub>3</sub> NCM83 cathode is the lowest among them, which is responsible for the highest capacity retention and the lowest polarization.

The degradations of NCM83 during cycling are probed with microscopic sight, and the results exhibit the morphology, surface composition, and crystal structure of the NCM83 change compared to its pristine status (Figure S20 of the Supporting Information). As shown in Figure 5a, the surface of the cycled bare NCM83 cathode becomes rough and covered with spotty species, indicating the thick cathode electrolyte interface (CEI) layers,<sup>45</sup> while for the 4Al–H<sub>2</sub>O NCM83 cathode, almost no spotty species occur, although the surface is still rough. The surface of the 4Al–O<sub>3</sub> NCM83 cathode is clean and smooth, indicating thin CEI layers. Figure 5b shows the F 1s spectra of the cycled NCM83 cathodes, and the F 1s peaks at 687.6 and 685.2 eV belong to PVDF and LiF, respectively,<sup>24</sup> which indicates that deleterious LiF is much less on the 4Al–H<sub>2</sub>O and 4Al–O<sub>3</sub> NCM83 cathodes than that on the bare NCM83 cathode, especially for the 4Al–O<sub>3</sub> NCM83 cathode. The ICP results from the anodes reflect the dissolved Ni ions from the cathodes during cycling. As shown in Figure 5c, the dissolved Ni ions from the 4Al–H<sub>2</sub>O or 4Al–O<sub>3</sub> NCM83 cathodes are remarkably less than those on the bare NCM83 cathode, especially for the 4Al–O<sub>3</sub> NCM83 cathode. The crystal structure of the cycled NCM83 cathode is characterized by XRD. As shown in Figure 5d, the XRD patterns of both the 4Al–H<sub>2</sub>O and 4Al–O<sub>3</sub> NCM83 cathodes show less full width at half maximum of peaks than the bare NCM83 cathode. Besides, the 4Al–O<sub>3</sub> NCM83 cathode shows

the most clearly separated (006)/(012) peak. The above results show that the 4Al–O<sub>3</sub> NCM83 cathode keeps the surface and crystal structure the best during the cycling, which indicates that the O<sub>3</sub>-based ALD Al<sub>2</sub>O<sub>3</sub> coatings give the best protection for the NCM83 cathode.

## 4. CONCLUSION

In summary, the process of H<sub>2</sub>O- and O<sub>3</sub>-based Al<sub>2</sub>O<sub>3</sub> ALD on NCM83 and their impacts on the electrochemical performance of NCM83 are revealed. C<sub>2</sub>H<sub>4</sub> is found as a special byproduct only produced during the TMA chemisorption on NCM83. *In situ* QMS and QCM results illustrate that the O<sub>3</sub>-based Al<sub>2</sub>O<sub>3</sub> ALD needs a longer growth period from the nuclei to continuous coatings than the H<sub>2</sub>O-based Al<sub>2</sub>O<sub>3</sub> ALD on NCM83 due to a lower nucleation and growth rate. The electrochemical test results indicate that the discontinuous Al<sub>2</sub>O<sub>3</sub> coatings give a good balance to the rate capability and cycling stability of the NCM83 cathode. At the same number of monolayers, the O<sub>3</sub>-based ALD Al<sub>2</sub>O<sub>3</sub> coatings give better rate and cycling performance to the NCM83 cathode than the H<sub>2</sub>O-based Al<sub>2</sub>O<sub>3</sub> coatings due to lower initial overpotential and overpotential accumulation during cycling. The characterizations of the cycled NCM83 cathodes exhibit the O<sub>3</sub>-based ALD Al<sub>2</sub>O<sub>3</sub> coatings giving fewer deleterious CEI layer growths and transition metal dissolutions and better crystal structure maintenance for the NCM83 cathode. This work provides a viable avenue to understand the H<sub>2</sub>O- and O<sub>3</sub>-based ALD Al<sub>2</sub>O<sub>3</sub> ALD growth process on NCM83 and rationally tune the monolayers of Al<sub>2</sub>O<sub>3</sub> on NCM83.

## ASSOCIATED CONTENT

### Supporting Information

The Supporting Information is available free of charge at <https://pubs.acs.org/doi/10.1021/acsami.4c15078>.

*In situ* QMS and QCM measurements of the Al<sub>2</sub>O<sub>3</sub> ALD process, ICP, XPS, TOF-SIMS, SEM, and XRD characterizations of the Al<sub>2</sub>O<sub>3</sub>-coated NCM83 particles, rate, cycling, and storage tests of the Al<sub>2</sub>O<sub>3</sub>-coated NCM83 cathodes, electronic conductivity of the Al<sub>2</sub>O<sub>3</sub>-

coated NCM83 particles, GITT, EIS, and DRT spectra of the  $\text{Al}_2\text{O}_3$ -coated NCM83 cathodes, and comparison of our work to literature reports ([PDF](#))

## AUTHOR INFORMATION

### Corresponding Authors

Xiao Liu – State Key Laboratory of Intelligent Manufacturing Equipment and Technology, School of Mechanical Science and Engineering, Huazhong University of Science and Technology, Wuhan, Hubei 430074, People's Republic of China;  [orcid.org/0000-0003-4178-5775](#); Email: [xiaoliu@hust.edu.cn](mailto:xiaoliu@hust.edu.cn)

Rong Chen – State Key Laboratory of Intelligent Manufacturing Equipment and Technology, School of Mechanical Science and Engineering, Huazhong University of Science and Technology, Wuhan, Hubei 430074, People's Republic of China;  [orcid.org/0000-0001-7371-1338](#); Email: [rongchen@mail.hust.edu.cn](mailto:rongchen@mail.hust.edu.cn)

### Authors

Jiawei Li – State Key Laboratory of Intelligent Manufacturing Equipment and Technology, School of Mechanical Science and Engineering, Huazhong University of Science and Technology, Wuhan, Hubei 430074, People's Republic of China

Jianhua Wu – State Key Laboratory of Intelligent Manufacturing Equipment and Technology, School of Mechanical Science and Engineering, Huazhong University of Science and Technology, Wuhan, Hubei 430074, People's Republic of China

Mingxuan Wang – State Key Laboratory of Intelligent Manufacturing Equipment and Technology, School of Mechanical Science and Engineering, Huazhong University of Science and Technology, Wuhan, Hubei 430074, People's Republic of China

Di Wen – State Key Laboratory of Intelligent Manufacturing Equipment and Technology, School of Mechanical Science and Engineering, Huazhong University of Science and Technology, Wuhan, Hubei 430074, People's Republic of China

Bin Shan – State Key Laboratory of Materials Processing and Die & Mould Technology, School of Materials Science and Engineering, Huazhong University of Science and Technology, Wuhan, Hubei 430074, People's Republic of China;  [orcid.org/0000-0001-7800-0762](#)

Complete contact information is available at:

<https://pubs.acs.org/10.1021/acsami.4c15078>

### Author Contributions

Jiawei Li proposed the idea, conducted the experiments, and wrote the original manuscript. Xiao Liu and Rong Chen supervised the project. Mingxuan Wang assisted in the visualization. Di Wen assisted in the experiments. Xiao Liu, Rong Chen, Bin Shan, and Jianhua Wu assisted in the discussions of the results. The manuscript was written through the contributions of all of the authors. All of the authors approved the final version of the manuscript.

### Notes

The authors declare no competing financial interest.

## ACKNOWLEDGMENTS

This work is supported by the National Key Research and Development Program of China (2022YFF1500400), the National Natural Science Foundation of China (52350349 and 52271216), and the New Cornerstone Science Foundation through the XPLORER PRIZE. The authors acknowledge the valuable suggestions from Hang Liu. The authors also acknowledge the technology support from the Analytic Testing Center and Flexible Electronics Research Center of Huazhong University of Science and Technology (HUST).

## REFERENCES

- (1) Kim, J.; Lee, H.; Cha, H.; Yoon, M.; Park, M.; Cho, J. Prospect and Reality of Ni-Rich Cathode for Commercialization. *Adv. Energy Mater.* **2018**, *8* (6), 1702028–1702052.
- (2) Wu, F.; Maier, J.; Yu, Y. Guidelines and trends for next-generation rechargeable lithium and lithium-ion batteries. *Chem. Soc. Rev.* **2020**, *49* (5), 1569–1614.
- (3) Xu, C.; Reeves, P. J.; Jacquet, Q.; Grey, C. P. Phase Behavior during Electrochemical Cycling of Ni-Rich Cathode Materials for Li-Ion Batteries. *Adv. Energy Mater.* **2021**, *11* (7), No. 2003404.
- (4) Song, C.; Moon, H.; Baek, K.; Shin, C.; Lee, K.; Kang, S. J.; Choi, N. S. Acid- and Gas-Scavenging Electrolyte Improving the Electrochemical Reversibility of Ni-Rich Cathodes in Li-Ion Batteries. *ACS Appl. Mater. Interfaces* **2023**, *15* (18), 22157–22166.
- (5) Park, C.; Lee, E.; Kim, S. H.; Han, J.-G.; Hwang, C.; Joo, S. H.; Baek, K.; Kang, S. J.; Kwak, S. K.; Song, H.-K.; Choi, N.-S. Malonic-acid-functionalized fullerene enables the interfacial stabilization of Ni-rich cathodes in lithium-ion batteries. *J. Power Sources* **2022**, *521*, No. 230923.
- (6) Yang, C.; Liao, X.; Zhou, X.; Sun, C.; Qu, R.; Han, J.; Zhao, Y.; Wang, L.; You, Y.; Lu, J. Phosphate-Rich Interface for a Highly Stable and Safe 4.6 V  $\text{LiCoO}_2$  Cathode. *Adv. Mater.* **2023**, *35* (14), No. 2210966.
- (7) Xu, H.; Li, Z.; Liu, T.; Han, C.; Guo, C.; Zhao, H.; Li, Q.; Lu, J.; Amine, K.; Qiu, X. Impacts of Dissolved  $\text{Ni}^{2+}$  on the Solid Electrolyte Interphase on a Graphite Anode. *Angew. Chem., Int. Ed.* **2022**, *61* (30), No. e202202894.
- (8) Zhao, Y.; Zheng, K.; Sun, X. L. Addressing Interfacial Issues in Liquid-Based and Solid-State Batteries by Atomic and Molecular Layer Deposition. *Joule* **2018**, *2* (12), 2583–2604.
- (9) Jiang, M.; Danilov, D. L.; Eichel, R. A.; Notten, P. H. L. A Review of Degradation Mechanisms and Recent Achievements for Ni-Rich Cathode-Based Li-Ion Batteries. *Adv. Energy Mater.* **2021**, *11* (48), No. 2103005.
- (10) Zou, Y.-G.; Meng, F.; Xiao, D.; Sheng, H.; Chen, W.-P.; Meng, X.-H.; Du, Y.-H.; Gu, L.; Shi, J.-L.; Guo, Y.-G. Constructing a stable interfacial phase on single-crystalline Ni-rich cathode via chemical reaction with phosphomolybdic acid. *Nano Energy* **2021**, *87*, No. 106172.
- (11) Du, Y.-H.; Sheng, H.; Meng, X.-H.; Zhang, X.-D.; Zou, Y.-G.; Liang, J.-Y.; Fan, M.; Wang, F.; Tang, J.; Cao, F.-F.; Shi, J.-L.; Cao, X.-F.; Guo, Y.-G. Chemically converting residual lithium to a composite coating layer to enhance the rate capability and stability of single-crystalline Ni-rich cathodes. *Nano Energy* **2022**, *94*, No. 106901.
- (12) Wang, M.; Feng, X.; Xiang, H.; Feng, Y.; Qin, C.; Yan, P.; Yu, Y. A Novel Protective Strategy on High-Voltage  $\text{LiCoO}_2$  Cathode for Fast Charging Applications:  $\text{Li}_{1.6}\text{Mg}_{1.6}\text{Sn}_{2.8}\text{O}_8$  Double Layer Structure via  $\text{SnO}_2$  Surface Modification. *Small Methods* **2019**, *3* (11), No. 1900355.
- (13) Zhao, Y.; Zhang, L.; Liu, J.; Adair, K.; Zhao, F.; Sun, Y.; Wu, T.; Bi, X.; Amine, K.; Lu, J.; Sun, X. Atomic/molecular layer deposition for energy storage and conversion. *Chem. Soc. Rev.* **2021**, *50* (6), 3889–3956.
- (14) Jung, Y. S.; Cavanagh, A. S.; Dillon, A. C.; Groner, M. D.; George, S. M.; Lee, S.-H. Enhanced Stability of  $\text{LiCoO}_2$  Cathodes in

- Lithium-Ion Batteries Using Surface Modification by Atomic Layer Deposition. *J. Electrochem. Soc.* **2010**, *157* (1), A75–A81.
- (15) Scott, I. D.; Jung, Y. S.; Cavanagh, A. S.; Yan, Y.; Dillon, A. C.; George, S. M.; Lee, S.-H. Ultrathin Coatings on Nano-LiCoO<sub>2</sub> for Li-Ion Vehicular Applications. *Nano Lett.* **2011**, *11* (2), 414–418.
- (16) Li, J.; Xiang, J.; Yi, G.; Tang, Y.; Shao, H.; Liu, X.; Shan, B.; Chen, R. Reduction of Surface Residual Lithium Compounds for Single-Crystal LiNi<sub>0.6</sub>Mn<sub>0.2</sub>Co<sub>0.2</sub>O<sub>2</sub> via Al<sub>2</sub>O<sub>3</sub> Atomic Layer Deposition and Post-Annealing. *Coatings* **2022**, *12* (1), 84.
- (17) Su, Y.; Cui, S.; Zhuso, Z.; Yang, W.; Wang, X.; Pan, F. Enhancing the High-Voltage Cycling Performance of Li-Ni<sub>0.5</sub>Mn<sub>0.3</sub>Co<sub>0.2</sub>O<sub>2</sub> by Retarding Its Interfacial Reaction with an Electrolyte by Atomic-Layer-Deposited Al<sub>2</sub>O<sub>3</sub>. *ACS Appl. Mater. Interfaces* **2015**, *7* (45), 25105–12.
- (18) Patel, R. L.; Xie, H.; Park, J.; Asl, H. Y.; Choudhury, A.; Liang, X. H. Significant Capacity and Cycle-Life Improvement of Lithium-Ion Batteries through Ultrathin Conductive Film Stabilized Cathode Particles. *Adv. Mater. Interfaces* **2016**, *3* (13), No. 1500046.
- (19) Li, W.; Cheng, D.; Shimizu, R.; Li, Y.; Yao, W.; Raghavendran, G.; Zhang, M.; Meng, Y. S. Artificial cathode electrolyte interphase for improving high voltage cycling stability of thick electrode with Co-free 5 V spinel oxides. *Energy Storage Mater.* **2022**, *49*, 77–84.
- (20) Khotimah, C.; Cheng, H.-M.; Wang, F.-M. Enhanced cyclability of lithium-ion batteries resulting from atomic layer deposition of Al<sub>2</sub>O<sub>3</sub> on LiFePO<sub>4</sub> electrodes. *J. Solid State Electrochem.* **2024**, DOI: 10.1007/s10008-024-05890-x.
- (21) Azaceta, E.; García, S.; Leonet, O.; Beltrán, M.; Gómez, I.; Chuvilin, A.; Mainar, A. R.; Blazquez, J. A.; Knez, M. Particle atomic layer deposition as an effective way to enhance Li–S battery energy density. *Mater. Today Energy* **2020**, *18*, No. 100567.
- (22) Zhang, X. F.; Belharouak, I.; Li, L.; Lei, Y.; Elam, J. W.; Nie, A. M.; Chen, X. Q.; Yassar, R. S.; Axelbaum, R. L. Structural and Electrochemical Study of Al<sub>2</sub>O<sub>3</sub> and TiO<sub>2</sub> Coated Li<sub>1.2</sub>Ni<sub>0.13</sub>Mn<sub>0.54</sub>Co<sub>0.13</sub>O<sub>2</sub> Cathode Material Using ALD. *Adv. Energy Mater.* **2013**, *3* (10), 1299–1307.
- (23) Gao, Y.; Park, J.; Liang, X. Comprehensive Study of Al- and Zr-Modified LiNi<sub>0.8</sub>Mn<sub>0.1</sub>Co<sub>0.1</sub>O<sub>2</sub> through Synergy of Coating and Doping. *ACS Appl. Energy Mater.* **2020**, *3* (9), 8978–8987.
- (24) Bao, W.; Qian, G.; Zhao, L.; Yu, Y.; Su, L.; Cai, X.; Zhao, H.; Zuo, Y.; Zhang, Y.; Li, H.; Peng, Z.; Li, L.; Xie, J. Simultaneous Enhancement of Interfacial Stability and Kinetics of Single-Crystal LiNi<sub>0.6</sub>Mn<sub>0.2</sub>Co<sub>0.2</sub>O<sub>2</sub> through Optimized Surface Coating and Doping. *Nano Lett.* **2020**, *20* (12), 8832–8840.
- (25) Lin, W.; Bao, W.; Cai, J.; Cai, X.; Zhao, H.; Zhang, Y.; Deng, Y.; Yang, S.; Zhou, Z.; Liu, Z.; Xie, J. Degradation of Nickel-Rich layered oxides in ambient air and its inhibition by surface coating and doping. *Appl. Surf. Sci.* **2023**, *615*, No. 156278.
- (26) Hsieh, C.-T.; Chao, C.-H.; Ke, W.-J.; Lin, Y.-F.; Liu, H.-W.; Gandomi, Y. A.; Gu, S.; Su, C.-Y.; Chang, J.-K.; Li, J.; Fu, C.-C.; Mallick, B. C.; Juang, R.-S. Roll-To-Roll Atomic Layer Deposition of Titania Nanocoating on Thermally Stabilizing Lithium Nickel Cobalt Manganese Oxide Cathodes for Lithium Ion Batteries. *ACS Appl. Energy Mater.* **2020**, *3* (11), 10619–10631.
- (27) Wang, W.; Lee, C.; Yu, D.; Kondo, Y.; Miyahara, Y.; Abe, T.; Miyazaki, K. Effects of a Solid Solution Outer Layer of TiO<sub>2</sub> on the Surface and Electrochemical Properties of LiNi<sub>0.6</sub>Co<sub>0.2</sub>Mn<sub>0.2</sub>O<sub>2</sub> Cathodes for Lithium-Ion Batteries through the Use of Thin-Film Electrodes. *ACS Appl. Energy Mater.* **2022**, *5* (4), 5117–5126.
- (28) Li, J.; Xiang, J.; Yi, G.; Hu, Z.; Liu, X.; Chen, R. Stabilization of the surface and lattice structure for LiNi<sub>0.83</sub>Co<sub>0.12</sub>Mn<sub>0.05</sub>O<sub>2</sub> via B<sub>2</sub>O<sub>3</sub> atomic layer deposition and post-annealing. *Energy Adv.* **2024**, *3* (7), 1688–1696.
- (29) Liu, X.; Li, Z.; Liao, X.; Hong, X.; Li, Y.; Zhou, C.; Zhao, Y.; Xu, X.; Mai, L. A three-dimensional nitrogen-doped graphene framework decorated with an atomic layer deposited ultrathin V<sub>2</sub>O<sub>5</sub> layer for lithium sulfur batteries with high sulfur loading. *J. Mater. Chem. A* **2020**, *8* (24), 12106–12113.
- (30) Xie, J.; Sendek, A. D.; Cubuk, E. D.; Zhang, X.; Lu, Z.; Gong, Y.; Wu, T.; Shi, F.; Liu, W.; Reed, E. J.; Cui, Y. Atomic Layer Deposition of Stable LiAlF<sub>4</sub> Lithium Ion Conductive Interfacial Layer for Stable Cathode Cycling. *ACS Nano* **2017**, *11* (7), 7019–7027.
- (31) Xie, J.; Zhao, J.; Liu, Y.; Wang, H.; Liu, C.; Wu, T.; Hsu, P.-C.; Lin, D.; Jin, Y.; Cui, Y. Engineering the surface of LiCoO<sub>2</sub> electrodes using atomic layer deposition for stable high-voltage lithium ion batteries. *Nano Res.* **2017**, *10* (11), 3754–3764.
- (32) Liu, W.; Li, X.; Xiong, D.; Hao, Y.; Li, J.; Kou, H.; Yan, B.; Li, D.; Lu, S.; Koo, A.; Adair, K.; Sun, X. Significantly improving cycling performance of cathodes in lithium ion batteries: The effect of Al<sub>2</sub>O<sub>3</sub> and LiAlO<sub>2</sub> coatings on LiNi<sub>0.6</sub>Co<sub>0.2</sub>Mn<sub>0.2</sub>O<sub>2</sub>. *Nano Energy* **2018**, *44*, 111–120.
- (33) Henderick, L.; Hamed, H.; Mattelaer, F.; Minjauw, M.; Meersschaut, J.; Dendooven, J.; Safari, M.; Vereecken, P.; Detavernier, C. Atomic Layer Deposition of Nitrogen-Doped Al Phosphate Coatings for Li-Ion Battery Applications. *ACS Appl. Mater. Interfaces* **2020**, *12* (23), 25949–25960.
- (34) Henderick, L.; Hamed, H.; Mattelaer, F.; Minjauw, M.; Nisula, M.; Meersschaut, J.; Dendooven, J.; Safari, M.; Vereecken, P.; Detavernier, C. Plasma enhanced atomic layer deposition of a (nitrogen doped) Ti phosphate coating for improved energy storage in Li-ion batteries. *J. Power Sources* **2021**, *497*, No. 229866.
- (35) Hoskins, A. L.; McNeary, W. W.; Millican, S. L.; Gossett, T. A.; Lai, A.; Gao, Y.; Liang, X.; Musgrave, C. B.; Weimer, A. W. Nonuniform Growth of Sub-2 Nanometer Atomic Layer Deposited Alumina Films on Lithium Nickel Manganese Cobalt Oxide Cathode Battery Materials. *ACS Appl. Nano Mater.* **2019**, *2* (11), 6989–6997.
- (36) Chen, L.; Warburton, R. E.; Chen, K.-S.; Libera, J. A.; Johnson, C.; Yang, Z.; Hersam, M. C.; Greeley, J. P.; Elam, J. W. Mechanism for Al<sub>2</sub>O<sub>3</sub> Atomic Layer Deposition on LiMn<sub>2</sub>O<sub>4</sub> from In Situ Measurements and Ab Initio Calculations. *Chem.* **2018**, *4* (10), 2418–2435.
- (37) Darapaneni, P.; Mane, A. U.; Turczynski, A.; Elam, J. W. Elucidating the Redox Behavior during Atomic Layer Deposition on Lithium-Ion Battery Cathode Materials. *Chem. Mater.* **2021**, *33* (20), 8079–8088.
- (38) Evenstein, E.; Rosy; Haber, S.; Sclar, H.; Houben, L.; Leung, K.; Leskes, M.; Noked, M. Atomic surface reduction of interfaces utilizing vapor phase approach: High energy LiNixMnyCoz oxide as a test case. *Energy Storage Mater.* **2019**, *19*, 261–269.
- (39) Kim, S. K.; Lee, S. W.; Hwang, C. S.; Min, Y. S.; Won, J. Y.; Jeong, J. Low temperature (<100°C) deposition of aluminum oxide thin films by ALD with O<sub>3</sub> as oxidant. *J. Electrochem. Soc.* **2006**, *153* (5), F69–F76.
- (40) Ha, S.-C.; Choi, E.; Kim, S.-H.; Sung Roh, J. Influence of oxidant source on the property of atomic layer deposited Al<sub>2</sub>O<sub>3</sub> on hydrogen-terminated Si substrate. *Thin Solid Films* **2005**, *476* (2), 252–257.
- (41) Kim, J. B.; Kwon, D. R.; Chakrabarti, K.; Lee, C.; Oh, K. Y.; Lee, J. H. Improvement in Al<sub>2</sub>O<sub>3</sub> dielectric behavior by using ozone as an oxidant for the atomic layer deposition technique. *J. Appl. Phys.* **2002**, *92* (11), 6739–6742.
- (42) Wang, H.; Liu, Y.; Liu, H.; Chen, Z.; Xiong, P.; Xu, X.; Chen, F.; Li, K.; Duan, Y. Effect of Various Oxidants on Reaction Mechanisms, Self-Limiting Natures and Structural Characteristics of Al<sub>2</sub>O<sub>3</sub> Films Grown by Atomic Layer Deposition. *Adv. Mater. Interfaces* **2018**, *5* (14), No. 1701248.
- (43) Caballero-Espitia, D. L.; Lizarraga-Medina, E. G.; Borbon-Núñez, H. A.; Contreras-Lopez, O. E.; Tiznado, H.; Marquez, H. Study of Al<sub>2</sub>O<sub>3</sub> thin films by ALD using H<sub>2</sub>O and O<sub>3</sub> as oxygen source for waveguide applications. *Opt. Mater.* **2020**, *109*, No. 110370.
- (44) Lin, C.; Zhang, Y.; Chen, L.; Lei, Y.; Ou, J.; Guo, Y.; Yuan, H.; Xiao, D. Hydrogen peroxide assisted synthesis of Li-Ni<sub>1/3</sub>Co<sub>1/3</sub>Mn<sub>1/3</sub>O<sub>2</sub> as high-performance cathode for lithium-ion batteries. *J. Power Sources* **2015**, *280*, 263–271.
- (45) Li, X.; Liu, J.; Banis, M. N.; Lushington, A.; Li, R.; Cai, M.; Sun, X. Atomic layer deposition of solid-state electrolyte coated cathode materials with superior high-voltage cycling behavior for lithium ion battery application. *Energy Environ. Sci.* **2014**, *7* (2), 768–778.